Quantifying the Evolution of Molecular Production Rates of comet 21P/Giacobini-Zinner with iSHELL/NASA-IRTF.

Faggi S. [1,2], Mumma M. J. [1], Villanueva G. L. [1], Paganini L.[3,2], Lippi M.[1,2]

[1] NASA Goddard Space Flight Center, 8800 Greenbelt Rd., Greenbelt, MD, 20771, USA

[2] American University, Dept. of Physics, 4400 Massachusetts Ave NW, Washington, DC 20016, USA

[2] NASA Headquarters, 4th street, Washington, DC 20546

Abstract

This paper presents results from our molecular characterization of comet 21P/Giacobini-Zinner during its 2018 apparition. We followed the comet during four observing runs, for a total of 8 nights. The high-resolution spectra of 21P were acquired using iSHELL - the near-IR high-resolution immersion echelle spectrograph on NASA/IRTF (Mauna Kea, Hawaii). We detected many cometary emission lines across four customized iSHELL settings in the (2.9 – 5.2) μm range. CO abundances relative to water displayed a relatively constant behavior during the observing campaign, suggesting a possible correlation between the outgassing of water and CO. While CO mixing ratios in 21P are consistent with the reference median value for Jupiter Family comets (JFCs), ethane was depleted relative to the reference median value for JFCs, excepting one observing run (8th and 9th Aug) in which ethane appeared overabundant. We consider several possible causes: an ethane outburst, decreasing outgassing of water, or a seasonal effect owing to nucleus rotation. In the pre-perihelion runs, methanol was overabundant compared with the reference median value for JFCs, however it decreased steadily to a depleted value during 21P's post-perihelion phase, suggesting a possible seasonal effect. We report 3-σ upper limits for acetylene, formaldehyde, ammonia and methane. The ratios of our measured 3-σ upper limits for acetylene and detections of hydrogen cyanide are consistent with the depletion of C_2 relative to CN in 21P observed at optical wavelengths. This result confirms that 21P is depleted in the carbon-chain primary volatile responsible for C_2 production.

1. Introduction

Comet 21P/Giacobini-Zinner is a short-period (P = 6.6 yr), Jupiter Family comet (T_j = 2.46) that was discovered in the early twentieth century by two astronomers almost simultaneously, Michael Giacobini and Ernst Zinner, from which the name.

Since its discovery, comet 21P/Giacobini-Zinner (hereafter 21P/G-Z) has been extensively observed throughout multiple perihelion passages. This comet is considered one of the brighter comets of its dynamical family and long-standing interest in it enabled the re-direction of ISEE-3 (Third International Sun-Earth Explorer) to intercept it in 1985; ISEE-3 was then renamed ICE (International Comet Explorer). The ICE mission was the first spacecraft aimed to fly through a cometary tail and study its properties, and at closest approach was ~ 7800 km from the nucleus. ISEE-3 was designed to conduct the first deep investigation of the interaction between the solar wind and the Earth's magnetic field, thus the spacecraft was mainly equipped with solar-wind plasma, magnetometer, cosmic-ray and high-energy particle experiments. The mission accomplished its primary goals in 1981 and began its re-direction to intercept the orbit of comet 21P/G-Z in June 1982, leading to the first *in situ* investigation of the magnetic properties and ions in a cometary tail (cf. Slavin et al. 1986a; Slavin et al. 1986b; Gloeckler et al. 1986; and many other papers in the Geophysical Research Letter and Science special issues). In support of the flyby mission, the cometary community conducted an extensive ground-based observing campaign spanning multiple spectral regions, at wavelengths from UV-optical (McFadden et al. 1987, Cochran and Barker 1987, Schleicher et al 1987) to near IR (Telesco et al 1986, Hanner et al. 1992) and radio (Gerard et al 1988). The collection of results from the ground-based observing campaign and the space mission observations delivered an extensive database for comet 21P/G-Z that has been improved with additional results from subsequent perihelion passages.

In 1995, A'Hearn *et al.* reported a comprehensive study of narrowband optical-UV photometry of 85 comets observed from 1976 to 1992. They proposed a possible classification of comets in two compositional groups, based on the relative abundances of product radicals C_2, C_3, CN, NH and OH: the *typical* and the *depleted* groups. About 30% of the analyzed comets appeared to be significantly depleted in C_2 and C_3 relative to CN, with respect to values found in the majority of the studied sample, leading to the denomination of the *carbon-chain depleted* taxonomical group[1]. Interestingly, most of the comets depleted in the carbon-chain molecules appeared to be originating from the Kuiper Belt and comet 21P/G-Z was described as the *prototype of the class*

[1] The carbon-chain species (C_2, C_3) relative to CN were depleted in G-Z by a factor of 20 relative to the mean value for the typical group. By contrast, the distribution of the abundance ratio of NH relative to CN did not show any particular correlation and was the same for both taxonomic groups (A'Hearn et al. 1995).

of carbon-chain depleted comets within the overall sample, due to its central position in the depleted group and its accurate measurements (see Fig. 10 in A'Hearn et al. 1995).

Comet 21P/G-Z was broadly studied during the following perihelion passages with different techniques, from imaging (e.g. Lara et al. 2003, Pittichova et al. 2008) to spectroscopy (e.g. Cochran et al. 1992, Fink 2009) and thanks to its brightness (and to the continuous improvement of instrumentation) was an optimal target to investigate such dichotomy in carbon-chain molecular abundance ratios with greater and greater detail and accuracy (Cochran et al. 1992). Since 1996, the commissioning of first CSHELL/NASA-IRTF and later NIRSPEC/Keck and CRIRES/VLT allowed the acquisition of high-resolution spectra of primary volatiles in comets, in the K-, L- and M-spectral regions, providing the unique capability to study organic trace gases and symmetric hydrocarbons together with water (cf. Mumma and Charnley 2011). In Table 1 we report a summary of near-IR high-resolution observations in previous apparitions and the list of detected molecular species. The orbital period of 21P/G-Z is not an integral multiple of Earth's, hence apparitions are not always favorable for Earth-based observations. The 2018 apparition was especially favorable (Fig. 1), offering the opportunity to test whether the dichotomy in carbon-chain depletion was reflected in both primary volatiles and radical product species, and thus to test the origins of fragment species.

Table 1. Previous near-IR high resolution observation of 21P/G-Z

Date	Instrument	Detected Molecules	R_h [au]	Δ [au]	$\dot{\Delta}$ [km/s]	Reference
2-10 Oct 1998	CSHELL NASA-IRTF	C_2H_6, CO	**1.25-1.19**	**1.08-1.03**	**~ -9.50**	Mumma et al. 2000
25-29 Oct 1998	CSHELL NASA-IRTF	H_2O, CH_3OH (3σ upper limits: C_2H_6, CO, C_2H_2, HCN, H_2CO)	**1.11-1.08**	**0.96-0.93**	**~ -8.50**	Weaver et al. 1999
3 June 2005	NIRSPEC Keck II	H_2O, CH_3OH, C_2H_6	**1.12**	**1.45**	**-5.40**	DiSanti et al. 2013
2012 Passage		- Not favorable-				
2018 Observing Campaign	iSHELL NASA-IRTF	H_2O, CO, C_2H_6, CH_3OH, C_2H_2, HCN, H_2CO	**1.17 – 1.01 – 1.09**	**0.60 – 0.39 – 0.49**	**(-13.36) – (-0.62) – (+10.66)**	This work

The commissioning of the high-resolution echelle spectrometer iSHELL/NASA-IRTF in August 2016 greatly improved the sensitivity of near-IR studies of comets [for instrumental details

and performances, see (Rayner et al. 2012)]. iSHELL offers a complete spectral sampling over a wider wavelength interval, at greatly improved spectral resolving power ($\lambda/\delta\lambda \sim 70{,}000$ at the smallest slit width, 0.375"). The instrument covers a wavelength region from 1.1 to 5.3 μm, with full spectral coverage per setting below 3.75 μm, and much higher sensitivity thanks to the new (2Kx2K) HAWAII-2 RG array. Moreover, iSHELL provides an updated slit-viewing camera that allows day-time on-source guiding, which was not possible with the previous instrumentation. The unique capability to guide during day-time improved our observing efficiency during G-Z's perihelion passage when the comet was more active and allowed us to detect molecules such as HCN and C_2H_2 that were previously only presented as 3σ-upper limit detections.

In this paper, we present our results from the favorable apparition of comet 21P/Giacobini-Zinner during its 2018 perihelion-passage, as revealed by iSHELL/NASA-IRTF.

2. Observations, Data Reduction, and brief description of the retrieval methodology

We observed comet 21P/G-Z using the near-IR high-resolution immersion echelle spectrograph iSHELL on the NASA/IRTF 3-m telescope. iSHELL has six different cross-dispersing gratings that allow the observer to select specific wavelength ranges within the full covered spectral range of about 1.1 - 5.3 μm. We generally used four different iSHELL settings customized by choosing an upper wavelength appropriate to optimally sample the targeted molecular species. We selected setting L1-c (upper wavelength 3.11 μm), setting L3 standard, setting Lp1 standard, Lp1c (upper wavelength 3.71 μm), and setting M1 standard. Details of our iSHELL custom-settings are also reported in Faggi et al. (2018). For the cometary observations, we used a slit width of about 0.75 arcsec, which corresponded to a nominal resolving power of about $\lambda/\Delta\lambda = 35{,}000$. In our cometary spectra, the detected emission lines (FWHM) were best fitted with different resolving powers depending on the general seeing conditions during the observing run. For the standard star observations, we used a slit width of 4 arcsec, in order to minimize the slit-loss and properly flux calibrate our spectra (except for the 30th July in which we used the 0.75 arcsec slit). We followed comet 21P/G-Z throughout the apparition, in four distinct observing runs as shown in Figure 1.

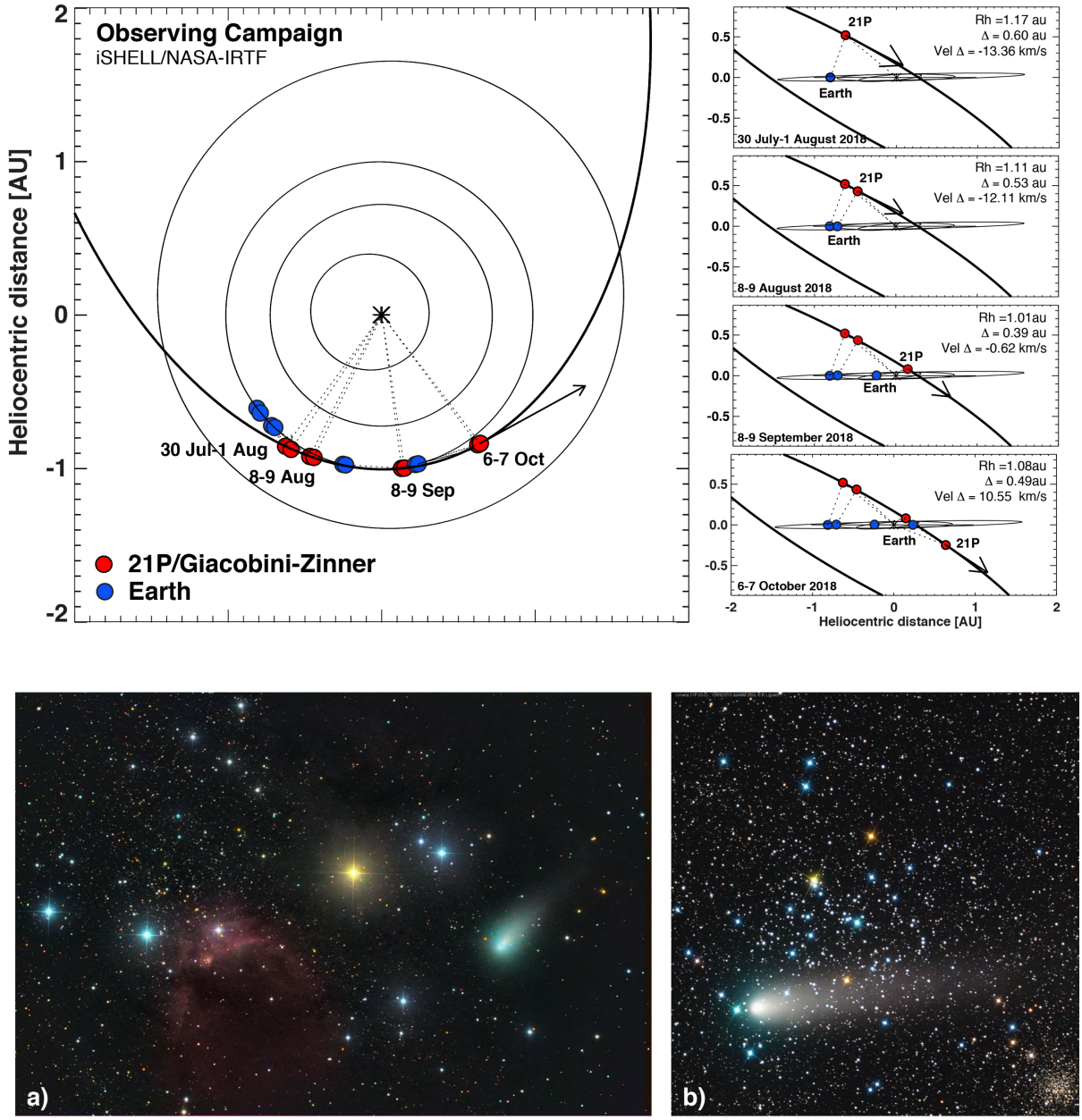

Figure 1 - Comet 21P/Giacobini-Zinner orbit diagram and visual aspect during the perihelion passage. The upper graphics show the top view and lateral views of the ecliptic plane and the orbit of comet 21P/Giacobini-Zinner during the 2018 observing campaign. For each observing run the position of comet 21P/G-Z (red) and the Earth (blue) are reported together with the dates of observations. The four right graphics report the mean cometary heliocentric distance R_h, the geocentric distance Δ, and geocentric velocity v= dΔdt or delta-dot, for each observing run. Bottom pictures show comet 21P/G-Z on 23 July (panel a) and on 15 September (panel b). Images credit: Rolando Ligustri.

The first two runs were in the pre-perihelion phase in late July and early August (specifically, 30th July – 1st August and 8th – 9th August), the third run was on 8th – 9th September close to the perihelion passage (which occurred on 10th September 2018), and the last run was in

the post-perihelion phase on 6th – 7th October 2018. The various heliocentric distances, geocentric distances, and geocentric velocities presented by 21P/G-Z during the observing campaign are reported both in Figure 1 and in Table 2, together with a summary of the observing log.

Table 2 – 21P/Giacobini-Zinner Observing Log

Date	UT [hh:mm]	Object name	Spectral Setting	Exposure Time [s], coadds	Time on Source [min]	Slit-wdth [arc-sec]	Airmass	R_h [au]	Δ [au]	$\dot{\Delta}$ [km/s]
Pre-perihelion Observations										
30 Jul	09:18 – 10:50	21P	L3	60.0, 1	68	0.75	2.088 – 1.654	1.172	0.604	-13.363
	11:15 – 11:20	HR8781	L3	20.0, 1		0.75	1.096 – 1.087	-	-	-
	11:27 – 11:36	HR8781	M1	10.0, 6		0.75	1.074 – 1.060	-	-	-
	12:04 – 13:20	21P	M1	10.0 ,6	64	0.75	1.488 – 1.424	1.172	0.604	-13.363
	13:43 – 15:40	21P	L1c	60.0, 1	88	0.75	1.421 – 1.541			
	16:00 – 16:10	HR8781	L1c	60.0, 1		0.75	1.399 – 1.455	-	-	-
1Aug	12:37 – 12:40	HR8781	M1	2.0, 5		4.0	1.004 – 1.004	-	-	-
	12:57 – 15:40	21P	M1	10.0, 6	120	0.75	1.455- 1.536	1.158	0.588	-13.086
8 Aug	08:26 – 08:37	HR8781	Lp1c	30.0, 2		4.0	1.765 – 1.657	-	-	-
	09:09 – 10:17	21P	Lp1c	60.0, 1	52	0.75	2.642 – 2.075	1.115	0.537	-12.5169
	10:21 – 10:52 11:26 – 12:18	21P	L1c	60.0, 1	64	0.75	2.047 – 1.855 1.747 – 1.598			
	10:59 – 11:10	HR8781	L1c	30.0, 2		4.0	1.062 – 1.047	-	-	-
9 Aug	10:56 – 13:09	21P	M1	10.0, 6	112	0.75	1.900 – 1.517	1.110	0.5304	-12.3918
	13:37 – 13:53	HR8781	M1	1.0, 60		4.0	1.063 – 1.093	-	-	-
	14:12 – 14:16	HR8781	Lp1	30.0, 2		4.0	1.134 – 1.146	-	-	-
	14:32 – 15:35	21P	Lp1	60.0, 1	48	0.75	1.457 – 1.481	1.110	0.5304	-12.3918
Perihelion Observations										
8 Sep	13:01 – 13:16	HR1641	L3	15.0, 4		4.0	1.463 – 1.395	-	-	-
	13:27 – 14:51	21P	L3	60.0, 1	64	0.75	1.493 – 1.173	1.013	0.392	-1.002
	15:09 – 15:59 16:32 – 18:18	21P	L1c	60.0, 1	116	0.75	1.134 – 1.066 1.045 –1.098			
	16:09 – 16:24	HR1641	L1c	15.0, 4		4.0	1.075 – 1.074	-	-	-
9 Sep	12:55 – 13:10	HR1641	Lp1c	15.0, 4		4.0	1.473 - 1404	-	-	-
	13:21 – 15:12	21P	Lp1c	60.0, 1	80	0.75	1.526 – 1.122	1.013	0.392	-0.624
	15:21 – 18:31	21P	L1c	60.0, 1	132	0.75	1.106 – 1.110			
	18:58 – 19:13	HR1641	L1c	15.0, 4		4.0	1.320 – 1.376	-	-	-
Post-perihelion Observations										
6 Oct	12:25 – 12:40	HR1641	Lp1c	15.0, 4		4.0	1.204 – 1.173	-	-	-
	12:53 – 14:12	21P	Lp1c	60.0, 1	60	0.75	1.893 – 1.344	1.080	0.487	10.443
7 Oct	12:44 – 12:55	HR1641	M1	3.0, 20		4.0	1.157 – 1.140	-	-	-
	13:14 – 15:07	21P	M1	10.0, 6	54	0.75	1.695 – 1.198	1.085	0.494	10.655

We adopted our standard ABBA nodding technique, sampling the comet signal alternatively in the A- and B- and following B- and A-beams, for all the observing runs except for the run close to the perihelion passage (8th – 9th September) in which iSHELL had a technical issue with the slit-length selector (the Dekker). The Dekker automatically sets the slit-length based on

the selected observing setting. For the L-, Lp- and M- settings usually the slit-length is 15 arcsec, but in the perihelion observing run the Dekker was stuck in the 5 arcsec slit-length position forcing us to use the off-slit nodding technique that it is usually adopted only in the shorter wavelength settings (J, H and K).

Each single order in a specific raw frame was cropped and processed separately. It was cleaned of bad pixels, straightened from the optical curvature and wavelength calibrated using our Goddard custom data reduction tools (Villanueva et al. 2013, Bonev et al. 2005, DiSanti et al. 2001) updated and tailored for iSHELL. We frequency-calibrated the spectra by fitting the terrestrial radiance with the Planetary Spectrum Generator (PSG, Villanueva et al. 2018). The flux calibration of the cometary spectra was obtained, order-by-order, applying the wavenumber-dependent conversion efficiency (Gamma, Γ_ν) derived from the comparison between the top-of-atmosphere stellar flux density (W m^{-2}/cm^{-1}), the modeled atmospheric transmittance, and the measured instrumental counts per pixel (ADU s^{-1}) at individual frequencies across the order.

We combined cometary signals from the A- and B- beams (except for the perihelion observing run in which we applied the off-slit nodding technique, where the signal was only in the A-beam), and we extracted cometary spectra over 15 spatial pixels along the slit, thus ±7 pixels from the nucleus centered position, defined from the spatial profile analysis as the central peak intensity. Details about iSHELL adopted plate scales along the slit for the different spectral settings are reported in Faggi et al. (2018) and in the iSHELL User's Manual – version 2018, while in Table 3 and Figure 2 we present the range of nucleus-centered regions spanned (in arcsec) and projected in the sky plane (km, at the comet's geocentric distance) during the observing campaign.

From the extracted spectra we retrieved rotational temperatures and molecular nucleus-centered production rates, applying the reliable methods that are well-documented in previous works: the *slope analysis* and the *correlation analysis*. Following the slope analysis approach, we compared the calibrated ro-vibrational line flux (corrected for the terrestrial transmittance at the Doppler-shifted line frequency) with the theoretical fluorescence efficiency (photons/molecule/s) computed from our quantum mechanical fluorescence models, at a specific T_{rot}(K) (DiSanti et al. 2006; Villanueva et al. 2011b, 2012a, 2012b, 2013a). In Table 4, we report a comprehensive summary of evaluated rotational temperatures and retrieved production rates of the detected molecules, during the entire perihelion passage. Examples of rotational analysis and correlation analysis are discussed in the following sections for water and organics.

To correct for slit-losses in the measured flux, introduced mainly by the atmospheric seeing, we derived the *growth-factor* (Q_{scale}) following the *Q-curve methodology* (Xie and Mumma 1996, Dello Russo et al. 1998, Mumma et al. 2003).

Table 3 – 21P/Giacobini-Zinner nucleus-centered sampled regions.

Date	Spectral Setting	Pixels[a]	Plate Scale[b] [arcsec]	d[c] [arcsec]	Δ [au]	r[d] [km]
30 Jul	L1c	15	0.167	±1.252	0.604	±549.763
	M1	15	0.165	±1.238	0.604	±543.616
	L3	15	0.187	±1.403	0.604	±616.068
1Aug	M1	15	0.165	±1.238	0.588	±529.215
8 Aug	L1c	15	0.167	±1.252	0.537	±488.779
	Lp1c	15	0.166	±1.245	0.537	±486.047
9 Aug	M1	15	0.165	±1.238	0.530	±477.014
	Lp1	15	0.166	±1.245	0.530	±479.711
8 Sep	L1c	15	0.167	±1.252	0.392	±356.799
	L3	15	0.187	±1.403	0.392	±399.832
9 Sep	L1c	15	0.167	±1.252	0.392	±356.799
	Lp1c	15	0.166	±1.245	0.392	±354.805
6 Oct	Lp1c	15	0.166	±1.245	0.487	±440.791
7 Oct	M1	15	0.165	±1.238	0.493	±443.713

a. Number of pixels along the slit, centered on the nucleus position from which we extracted the cometary spectra
b. Adopted mean plate scales in the cross-disperser direction. Measurements are reported in the iSHELL User's Manual and accurate to about ±0.005 arcsec
c. Spanned arcsecond along the slit
d. Corresponding projected distance in the coma from the nucleus position, measured orthogonal to the geocentric direction.

This correction factor (Q_{scale}) is defined as the inverse ratio between the *nucleus-centered production rate* (Q_{nc}) and a *terminal production rate* (Q_{term}) evaluated for the detected emission lines by analysis of their spatial profiles along the slit. For 21P/G-Z we computed the growth-factors from the brightest lines in our spectra, among the different iSHELL spectral settings. We defined boxes of 25 pixels (5 pixels in the spatial direction × 5 pixels in the spectral direction) from which we evaluated the spherical production rates, Q_i. Each spherical production rate was extracted at intervals of 5 pixels stepped along the slit, starting at ±2 pixels from the central position. The nucleus-centered production rate Q_{nc} is derived as combination of (Q_{-1}, Q_0, Q_1), reported as the grey shadowed boxes in Figure 2, and spanning 15 pixels (the central pixel and ±7 pixels upward and downward along the slit starting from the centered pixel). The terminal production rates were obtained by comparing (Q_{-3}, Q_{-2}, Q_{-1}, Q_0, Q_1, Q_2, and Q_3), except for the third run (8^{th} – 9^{th} September) close to the perihelion passage, in which iSHELL offered only 5 arcsec slit length. In that run we extracted the terminal production rates by comparing (Q_{-2}, Q_{-1}, Q_0, Q_1, and Q_2). For each observing run, we derived a distinct growth factor for each setting, as the

weighted mean of the growth factors evaluated on the brightest molecular lines in each order. Growth factors are reported in Table 4 along with the computed total molecular production rate for each species. The global production rates (Q_{tot}) for primary volatiles detected in 21P/G-Z were scaled from the nucleus-centered values with the following formalism: $(Q_{tot}) = (Q_{scale})^* (Q_{nucl})$.

In Figure 2 we show the spatial profiles for the brightest lines of several species, from which we computed growth-factors.

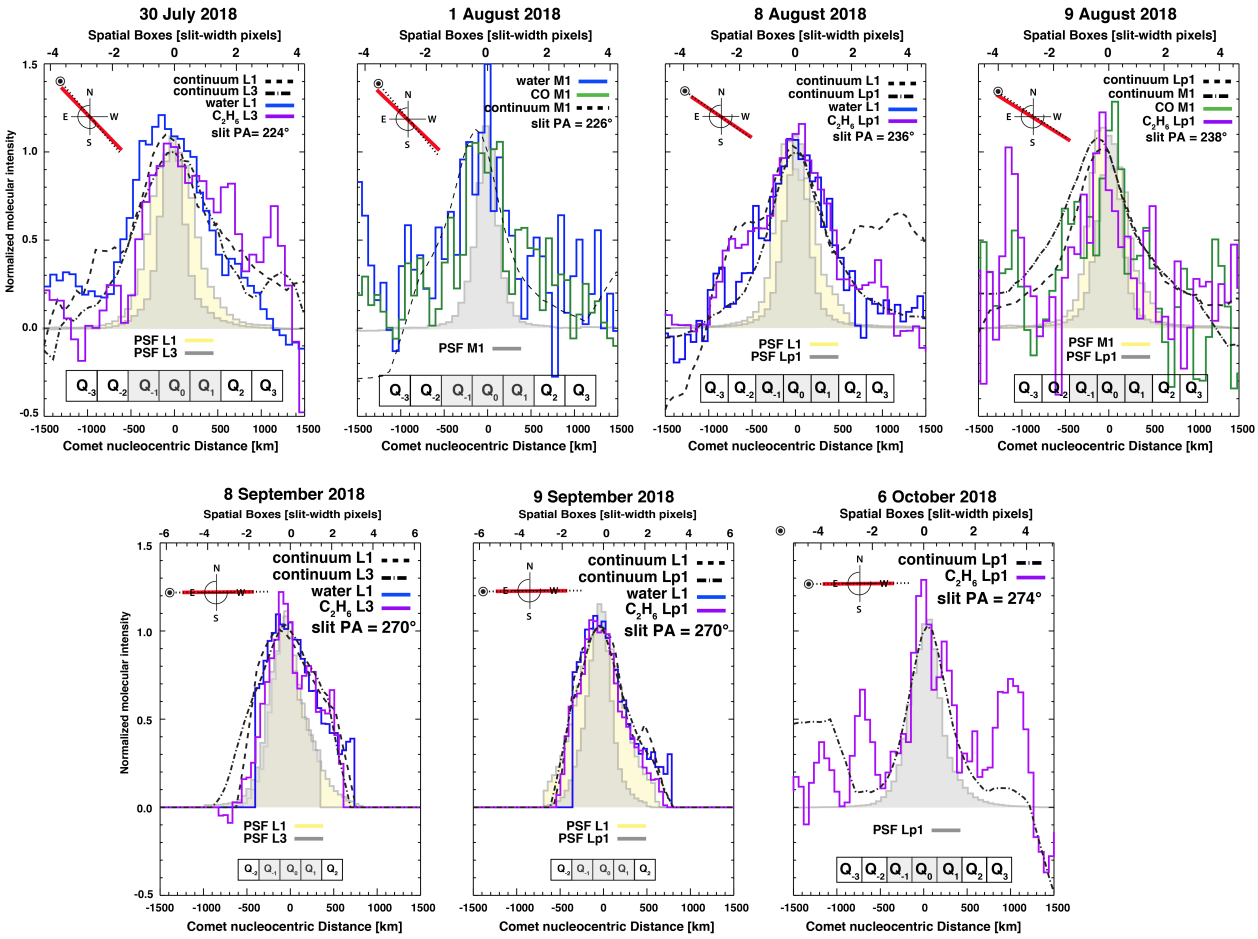

Figure 2. Spatial profiles measured for the brightest lines of water, ethane and carbon monoxide in 21P/Giacobini-Zinner during this observing campaign. The normalized molecular intensity (y-axis, relative units) is reported with respect to the nucleus-centered distance (x-axis, units of km and spaxels (slit-width pixels)). Inside the panels, we show the spatial boxes that define the integration area in which we computed the nucleus-centered and the terminal production rates and from which we evaluated the growth factor for each setting. The spatial box (Q_0) is located at the center of the peak of continuum intensity as determined by the spatial analysis and it spans 5×5 pixels. In the panels the outgassing profile for multiple molecular volatiles are shown in different colors and compared to the cometary continuum profile (dashed black lines) of each setting. The full light grey and yellow profiles represent the PSF measured on the star for different settings, and represents the quality of the seeing during our observations. The Sun position angle and the slit position angle (in red) are shown on the upper left corner of each panel.

The spatial profiles of water, C_2H_6 and CO are shown for the three observing runs (30th July, 1st August, 8th – 9th August four upper panels, 8th – 9th September and 6th October bottom

three panels). The continuum profile (dashed lines) is computed as the weighted mean of the continuum spatial profiles extracted for each order of a specific setting; the PSF for the star is also shown (light grey and yellow). 21P/G-Z spatial profiles do not show any particular anisotropy, within the poor signal-to-noise. We achieved higher SNRs during the third observing run, close to perihelion passage, but the shorter slit-length prevented a proper spatial analysis; despite this inconvenience, the molecular outgassing profiles follow the dust profiles and look symmetric.

Table 4 – Retrieved rotational temperatures, production rates, and mixing ratios for primary volatiles in 21P/Giacobini-Zinner.

Date	Molecule	Spectral Setting	T_{rot}[a] [K]	Q_{nucl}[b] [10^{25} s^{-1}]	Seeing[c] [arcsec]	Q_{scale}	Q_{tot} [10^{25} s^{-1}]	Mixing ratio[d] [%]
30 Jul	H_2O	L1c	[50]	1491.45 ± 120.14	0.24 – 1.45 [0.8] on L1c	1.54±0.19	2401.24 ± 393.81	
		M1	[50]	1546.62 ± 187.73		1.61±0.23	2279.23 ± 369.12	
		L1c+M1	[50]				2316.08 ± 300.47	100
	CO	M1	50 ± 10	34.30 ± 5.01		1.61±0.23	55.22 ± 11.28	2.38 ± 0.39
	C_2H_6	L3	[50]	3.10 ± 0.51		1.45±0.38	4.49 ± 1.45	0.19 ± 0.07
	CH_3OH		[50]	45.83 ± 5.49			66.45 ± 19.98	2.87 ± 0.94
	CH_4		[50]	< 14.28			< 20.71	< 0.89
	HCN	L1c	[50]	< 2.08		1.54±0.19	< 3.20	< 0.14
	C_2H_2		[50]	< 2.93			< 4.52	< 0.20
	NH_3		[50]	< 41.38			< 63.72	< 2.75
1Aug	H_2O	M1	56 ± 15	2108.30 ± 165.15	0.38 – 1.67 [0.8] on M1	1.51±0.12	3187.72 ± 355.24	100
	CO		[55]	41.21 ± 4.03			62.22 ± 7.84	1.95 ± 0.33
8 Aug	H_2O	L1c	60 ± 18	1063.86 ± 65.07	no data MKWC [0.9] on L1c	1.61±0.07	1707.77 ± 128.77	100%
	HCN		[60]	< 1.16			< 1.87	< 0.11
	C_2H_2		[60]	< 1.76			< 2.83	< 0.17
	NH_3		[60]	<3 1.50			< 50.72	< 2.97
	C_2H_6	Lp1c	[60]	7.77 ± 0.81		1.39±0.21	8.61 ± 1.63	0.50 ± 0.10
	CH_3OH		[60]	40.81± 3.63			57.13 ± 10.31	3.35 ± 0.65
	CH_4		[60]	< 31.98			< 44.77	< 2.62
	H_2CO		[60]	< 1.85			< 2.60	< 0.15
9 Aug	H_2O	M1	[60]	772.61 ± 175.07	no data MKWC [0.6] on Lp1c	1.38±0.39	1066.21± 396.21	100
	CO		[60]	17.13 ± 3.29			23.65 ± 8.08	2.22 ± 1.10
	C_2H_6	Lp1	[60]	7.61 ± 1.26		1.38±0.84	8.52 ± 2.95	0.80 ± 0.40
	CH_4		[60]	< 21.49			< 29.77	< 2.78
	H_2CO		[60]	< 2.41			< 3.33	< 0.31
	CH_3OH		[60]	31.03 ± 6.22			42.83 ± 14.83	4.02 ± 2.01
8 Sep	H_2O	L1c	76 ± 1	1713.79 ± 13.24	0.19 – 1.86 [0.8] on L3 [0.9] on L1c	1.62±0.03	2776.33 ± 557.10	100
	HCN		76 ±5	2.28 ± 0.19			3.68 ± 0.31	0.13 ± 0.01
	NH_3		[75]	< 0.24			< 13.34	< 0.48
	C_2H_2		[75]	< 0.41			< 0.67	< 0.02
	C_2H_6	L3	[75]	3.95 ± 0.38		1.51±0.17	5.97 ± 0.88	0.22 ± 0.03
	CH_3OH		[75]	24.89 ± 3.71			37.59 ± 7.02	1.35 ± 0.25
9 Sep	H_2O	L1c	77 ± 1	1590.00 ± 20.64	no data MKWC [0.9-1] on L1c	1.65±0.03	2623.51 ± 586.06	100
	HCN		[75]	2.60 ± 0.19			4.30 ± 0.32	0.16 ± 0.01
	NH_3		[75]	< 7.63			< 12.59	< 0.48
	C_2H_2		[75]	< 0.37			< 0.62	< 0.02
	H_2CO	Lp1c	[75]	< 0.81		1.47±0.22	< 1.19	< 0.05
	C_2H_6		[75]	5.64 ± 0.41			8.30 ± 1.38	0.32 ± 0.05
	CH_3OH		[75]	24.11 ± 2.18			35.44 ± 6.20	1.35 ± 0.24

6 Oct	C_2H_6	Lp1c	[65]	2.90 ± 0.63	0.24 – 0.89 [0.8]	1.57±0.36	4.55 ± 1.44	0.18 ± 0.08
	CH_3OH		[65]	11.81 ± 1.42			18.53 ± 4.80	0.69 ± 0.29
	CH_4		[65]	< 18.90			< 26.46	< 1.02
	H_2CO		[65]	< 0.86			< 1.35	< 0.05
7 Oct	H_2O	M1	[65]	1467.78 ± 491.01	[1.0]	1.89±0.64	2583.30 ± 864.18	100
	CO		[65]	19.37 ± 5.34			37.18 ± 15.93	1.44 ± 0.78

a) To compare molecular production rates, we decided to lock the rotational temperatures to a value based on the most sensitive measurement for that night. Adopted T_{rot} are reported in squared brackets. Rotational temperatures were obtained using the excitation analysis method, and when the derived confidence limits (±1σ) were less than 20 K we use them to lock T_{rot} for that night. We could not derive precise rotational temperatures in the post perihelion phase, owing to the low SNR and reduced number of detected lines, so we adopted a T_{rot} of 65 K.
b) Detections lower than 3-σ are reported here as (3-σ) upper limits. Their measured levels and confidence limits are given in the on-line material.
c) The range of seeing values presented here are taken from the Mauna Kea Weather Center (MKWC) website. The minimum and maximum seeing value during the observing night are also reported. We also report seeing values from our data (squared brackets), based on the PSF of a focus star measured before starting a cometary observing setting.
d) Mixing ratios relative to measured water are reported.

3. Results and Discussion

3.1 Water production rates across the perihelion passage

We detected multiple water emission lines in setting M1 and L1c in all four observing runs. In L1c during the perihelion passage, we identified 71 water lines from seven vibrational non-resonance fluorescence bands: (101-001), (200-001), (201-200), (200-100), (101-100), (110-010) and (111-110) on 8th September, and 68 water lines from eight vibrational non-resonance fluorescence bands: (101-001), (200-001), (201-200), (200-100), (101-100), (110-010), (111-110) and (111-011) on 9th September[2]. In Figure 3 upper plots, we present two fully analyzed cometary spectra showing water emission lines, as examples. In panel a), identified water emission lines extracted from order 111 of M1 setting on 1st August 2018 are shown together with detected CO lines, while in panel b) ortho- and para- water lines from order 181 of L1c setting on 8th September are presented together with an OH doublet. In both panels, the continuum affected by terrestrial atmospheric transmittance, is synthesized with PSG and shown in gray (superimposed and also below).

[2] On 8th September we detected 8 lines that we didn't observe on the 9th and specifically at 3319.48, 3346.61, 3387.54, 3415.77, 3439.43, 3549.84, 3539.51, and at 3549.84 [cm^{-1}]
On 9th September we detected 4 lines that we didn't see on the 8th and specifically at 3347.92, 3429.84, and at 3445.90 [cm^{-1}].

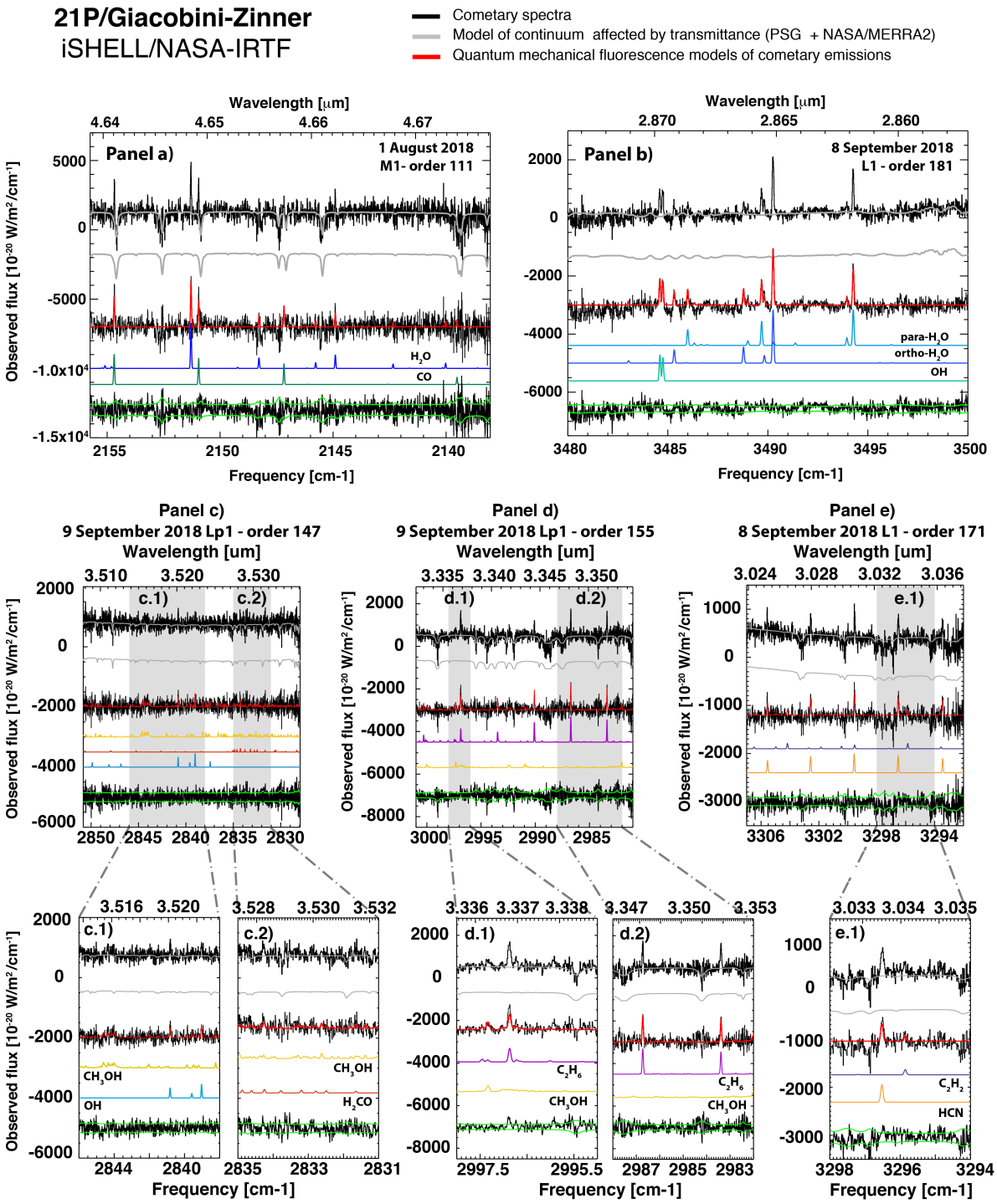

Figure 3 –Extracted Spectra for 21P/Giacobini-Zinner and Excitation Analysis.
Panels show cometary spectra extracted from specific orders of the four iSHELL echellograms. Cometary spectra are shown and compared with optimized synthetic spectra for detected species. The modeled emission spectra are shown shifted downward along the y-axis relative to the residual cometary spectrum, for clarity. The lowest trace in each panel is the grand residual after subtracting the modeled emissions from the measured molecular residual; the expected stochastic noise envelope (±σ) is shown in light green. Panels f, g, and h show the emission lines detected in zoomed portions of the spectral orders in panels c, d, and e (highlighted by grey boxes).

Examples of cometary molecular residuals (after continuum subtraction) and of the modeled spectra for fluorescent emission from detected molecules (ortho-H_2O, para- H_2O, CO, and OH) are reported individually in the middle traces of the graphic (using different colors) and also from all molecules (superimposed, red). The lowermost trace shows the spectral residuals after subtracting the modeled molecular detections and continuum; the ±1σ error level is displayed in light green. The observed fluxes (W m^{-2}/cm^{-1}) are shown with respect to frequency (cm^{-1}) and wavelength (μm). The scale of the x-axis is shown in frequency (cm^{-1}) below each panel and in wavelength (μm) above each panel.

In Figure 4 we present an example of water rotational excitation analysis performed on 8th September during the perihelion passage. In panel a) the slope analysis method is shown. The x-axis represents the mean ground-state rotational energy (cm^{-1}) of the principal pumping transitions for an individual line and the y- axis represents the molecular production rate ($Q(H_2O)$ in units of 10^{29} s^{-1}) extracted from any individual line. Ortho- and para-water lines are shown in two different shades of blue. We evaluated the water rotational temperature by graphing the observed and predicted flux ratio vs. the mean value of pumping rotational state energies in the ground vibrational state, for each line. The emitted line fluxes depend on the populations of rotational levels in the upper vibrational state (E_{up}) that in turn reflect the temperature-dependent distribution of the ground state; measurements of individual emission lines that span a wide range of ground-state excitation energies (along with state-of- the-art line-by-line emission models with full fluorescence cascade) are used to provide accurate retrievals. In retrieving nucleus-centered production rates, we accounted for the fraction of total coma molecules sampled by the beam under the assumption of spherically symmetric outflow at uniform velocity. The values obtained for rotational temperatures and nucleus-centered production rates during the overall observing campaign are reported in the fourth and fifth columns of Table 4. In Figure 4 (panel b), we compare the water rotational temperature derived from the slope analysis method (purple) and from the correlation analysis method (light green). The x-axis represents the rotational temperature, T_{rot} (K). The left y-axis reports the scale for the correlation coefficient while the right y-axis reports the scale for absolute values of slope (in units of 10^{-3}).

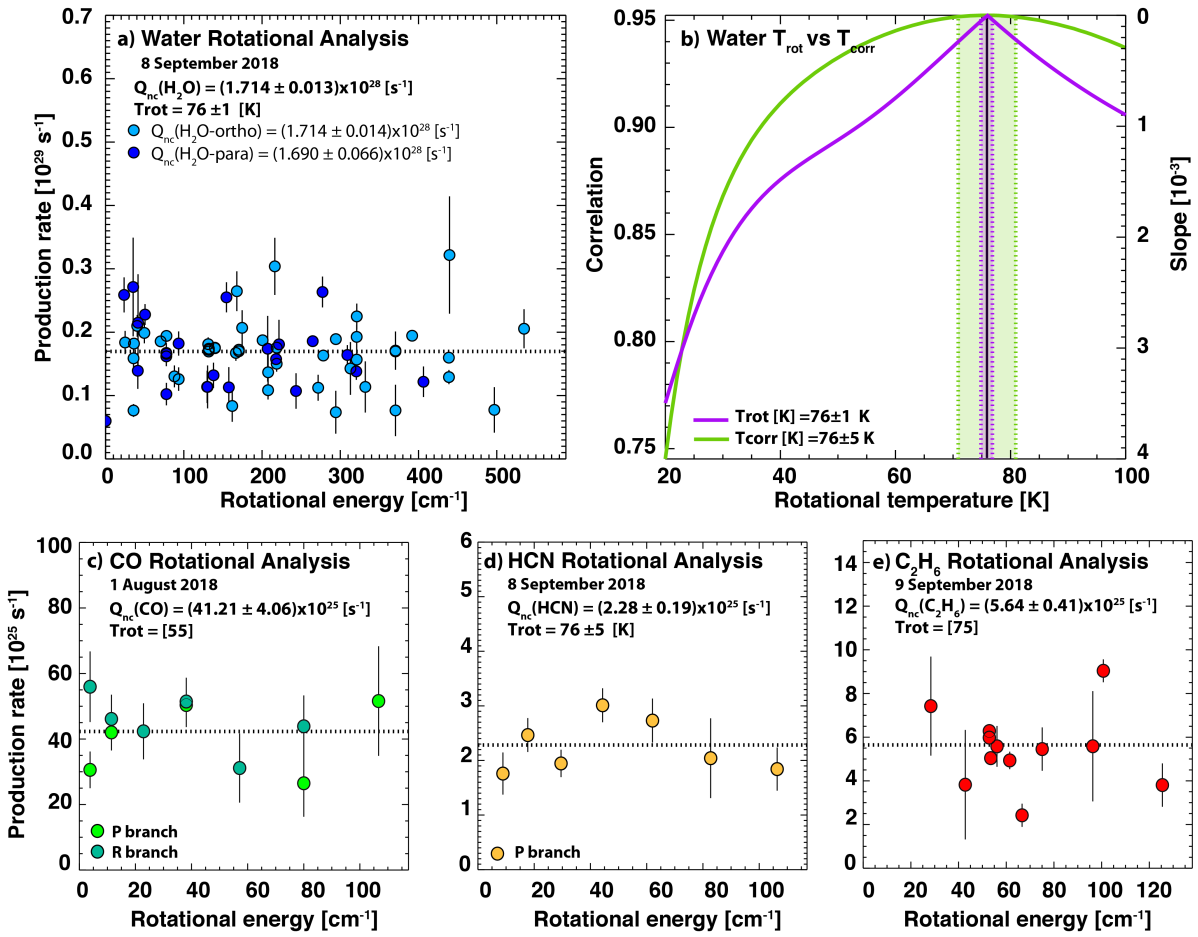

Figure 4 –Rotational temperature and production rate analyses for water and organic trace gases in 21P/Giacobini-Zinner.
Panels a), c), d) and e) show the excitation analysis for water and HCN, both in settings L1-c (on 8th September), for CO in setting M1 (on 1st August 2018), and for C_2H_6 in setting Lp1 (on 9th September 2018). The comparison of the water rotational temperatures, retrieved on 8th September, derived from the slope analysis method (purple) and from the correlation analysis method (light green) is reported in panel b).

On 8th September, during the perihelion passage, our measured ortho-to-para ratio is (3.04 ± 0.12), leading to a spin temperature $T_{spin} > 39$ K. This result suggests 21P cometary embryos may have aggregated in a warm formation region. Kawakita et al. found a similar conclusion from their observed spectra at N-band in which both crystalline olivine and crystalline pyroxene features were clearly detected, leading to a high fraction of crystalline-to-amorphous silicate grains, indicating a possible warm birthplace for such grains. (Kawakita et al. 2018). A dedicated paper about OPRs in comets will be released soon including a detailed discussion of ortho-to-para ratios measured in 21P/G-Z across the perihelion passage, and their meaning (Faggi et al., in prep.).

The retrieved total production rates for water and several trace gases during the observing campaign, obtained after slit-loss correction, are reported numerically in the next-to-last column

of Table 4 and graphically in Figure 5 (panel A). The y- axis represents the total species production rates [e.g., Q(H_2O)] in units of [s^{-1}], and the x-axes report the observation dates [dd/mm] and the days before the perihelion passage. Water measurements in L1 setting and M1 setting are shown in two different shades of blue dots.

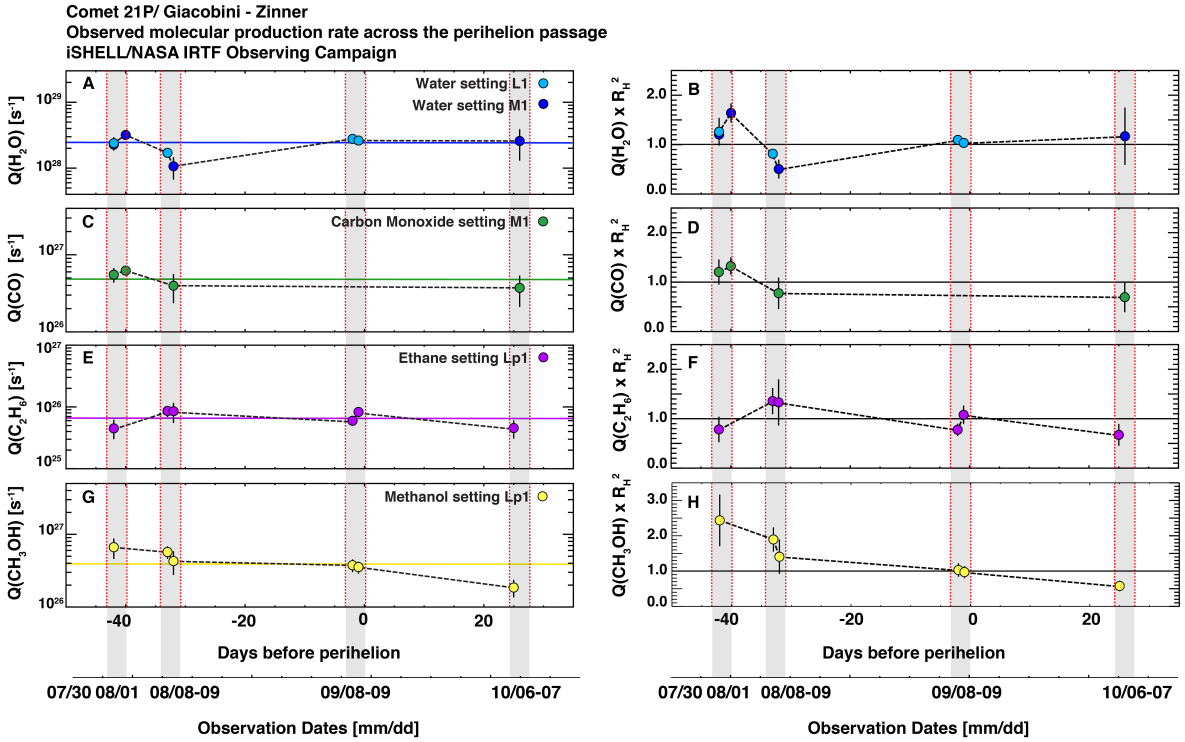

Figure 5 –Overview of Molecular Production Rates in 21P/Giacobini-Zinner.
In the graphics, each color is distinctive of a specific molecule. Water is represented (panels A and B) in two different shades of blue according to the different iSHELL settings in which it was measured. We show CO in green (panel C and D), ethane in purple (panel E and F), and methanol in yellow (panel G and H). For each molecule, the left panels (e.g., A, C, E, G) present the total molecular production rates retrieved during the observing campaign, while the right panels (e.g. B, D, F, H) show the outgassing variability after correcting for insolation (these represent the specific production rates relative to perihelion values, cf. Mumma et al. 2003). The values are normalized to the weighted mean value for each species.

It is possible to note that water looks almost constant within the confidence limits, except for some variability during the pre-perihelion observing runs. Based on our measured production rates during the observing campaign, and assuming that the cometary outgassing depends on the insolation (as R_h^{-2}), we decided to compute the product [Q(H_2O) × R_h^2] that removes orbital variations in insolation and reveals the "specific molecular production rate" (this concept/nomenclature was introduced by Mumma et al. 2003). In Figure 5 (panel B), we show this quantity for water normalized to the value measured during perihelion passage, when we had the most accurate results. The graphic in panel B shows clearly that specific water outgassing in early

August exceeded the most accurate measurements we performed in September by about 49%. This increase was followed a week later, on 8th-9th August, by a decrease of about 54%, relative to the September measurement. This observed intrinsic water variability is in agreement with the scenario of a general heterogeneous outgassing behavior of 21P/G-Z, claimed from previous chemical investigations. Water variability observed during the 2018 perihelion passage could explain the inconsistencies registered in past water measurements performed back in the 1998 passage. During the 1998 perihelion approach indeed, water was not detected in the early October observations performed with CSHELL/NASA-IRTF (Mumma et al. 2000), but it was detected three weeks later during observations performed with the same instrument (Weaver et al. 1999).

3.2 Organics production rates and their molecular abundances

Together with water, we identified and characterized eight organic molecular species: CO, C_2H_6, CH_3OH, HCN, C_2H_2, H_2CO, CH_4 and NH_3 along with prompt emission (OH*) from the radical OH. CO emissions were detected mostly in orders 110, and 111 of setting M1, together with water. An example of CO emission lines is presented in Figure 3, panel a). Methanol was generally detected in setting Lp1-c and L3, in orders 154 and 155 together with ethane. Hydrogen cyanide was identified in order 170, 171 and 173 of setting L1c together with 3-σ upper limits for acetylene and ammonia. Formaldehyde (3-σ) upper limits were reported for order 143, 144, 145, and 147 of setting Lp1 (Lp1-c). Methane (3-σ) upper limits were reported for order 155, 157 and 158 of setting Lp1-c (Lp1), and order 157, 158 of setting L3.

Examples of calibrated and analyzed spectra are presented in Figure 3, middle three graphics (panel c, d, e), and corresponding zoomed panels below (c.1, c.2, d.1, d.2, and e.1). As previously described for the water spectra, identified emission lines extracted from order 147 and 155 of Lp1 setting on 9th September 2018 and from order 171 of L1c setting on 8th September are presented. Again, the continuum modeled with PSG, is shown in gray (superimposed and below), while the cometary molecular residuals (after continuum subtraction) and the synthetic spectra for fluorescent emissions of C_2H_6, CH_3OH, HCN, C_2H_2, H_2CO, and OH are reported in the middle traces of the graphic (using different colors) and also superimposed (all molecules, red).

The slope and correlation analysis methods (see §2.2) were applied to the six trace molecular species detected across these four settings of iSHELL. To evaluate molecular nucleus-centered production rates, we extracted rotational temperatures (T_{rot}) for the spectra centered on

the nucleus position (see §2.1). In Figure 4, panel c), d) and e), the rotational analysis of three different molecules: CO, HCN and C_2H_6, are shown as explanatory examples. In retrieving production rates and molecular abundances, when confidence limits were not sufficiently accurate (i.e., when the uncertainty in T_{rot} exceeded 20K (1-σ)), we adopted a fixed rotational temperature corresponding to the most accurate rotational temperature retrieved for that date. In Table 2, the retrieved nucleus-centered molecular production rates are reported for all species, along with the growth factors and the slit-loss-corrected production rates.

Organic molecular abundances relative to water and 3-σ upper limits are also reported numerically in Table 4 and are discussed in detail in the next sections.

3.2.1 The hypervolatiles in 21P/G-Z: CO, CH_4 and C_2H_6

Carbon monoxide is one of the most hyper-volatile species detected in the cometary coma. It has an important role as indicator of the thermal evolution and formation history of cometary nuclei. Due to its low sublimation temperature (~ 24 K, Yamamoto et al. 1985), CO enrichment or depletion in comets can provide important constraints on the processing that occurred in the birthplace of pre-cometary ices (e.g. the discussion for Oort cloud comets in Paganini et al. (2014). Of the hyper-volatile candidates targeted in 21P, sensitive upper limits were obtained for CH_4, (see §3.2.3) – we achieved clear detections only of CO and C_2H_6.

We detected carbon monoxide in 21P/G-Z in the pre-perihelion observations of 31st July, 1st August and 9th August, and in the post-perihelion phase on 6th October, when the comet had a geocentric velocity sufficient to shift the cometary emission lines from their telluric counterparts (see observation log in Table 2). Absolute values of CO production rates are presented in Figure 5, panels C and D, and its abundances relative to water in Figure 6, panel (a). Interestingly, a possible correlation between CO and water outgassing is observed in the absolute values of total molecular production rates. Even if based on few measurements, we note that CO seems to follow the water trend: it appears pretty much constant in time except for a slight increase in early August followed by a decrease during our second pre-perihelion run. The limited number of consecutive observing nights restricts a full evaluation of chemical production and possible variations, but our data suggest a possible correlation between water and CO outgassing. Indeed, CO mixing ratios are practically constant throughout the observing campaign within confidence limits (Figure 6).

On the other hand, ethane and methanol do not share this behavior, given that they vary in a different way.

The correlation between H_2O and CO is quite interesting considering their distinct *polar* (H_2O) and *apolar* (CO) natures. The formation of apolar ice layers on the mantle of interstellar grains occurs at substantially lower temperatures than polar ice layers (Ehrenfreund and Schutte 2000), so this correlation observed in our mixing ratios could be a hint of a possible homogeneous composition of material in the 21P nucleus at the macro-molecular level, i.e. CO and H_2O condensed together on icy grains at very low temperatures. In Figure 6, CO mixing ratios in 21P/G-Z are compared with the median reference value for JFCs [CO_{JFC} = 1.77, black line] and with the median reference value among all sampled comets (hereafter "all") [CO_{all} = 2.18, blue line]. When defining "reference" values, in this work we consider the "median" of values reported in the recent literature, instead of the straight average (or mean), since in most cases cometary abundances do not follow a normal/gaussian distribution (e.g., Bockelee-Morvan and Biver 2017, Fig. 3 and Dello Russo et al. 2016, Fig. 2). Furthermore, the median value is more immune to outliers and better captures the typicality of a population. We calculated median values for mixing ratios in JFCs using data for 10 comets compiled by Paganini et al. 2019 (Table 3). Reference values for mixing ratios in "all" comets are the median values calculated from mixing ratios for Oort Cloud Comets (OCCs) reported in a recent paper on taxonomic studies of 30 comets (Dello Russo et al. 2016, Table 3) and for JFCs from Paganini et al 2019, ["all" = OCCs + JFCs]. In Table 5, median reference values are reported. As can be seen in the Figure 6, CO in 21P/G-Z is consistent with the median mixing ratio in JFCs, and with respect to the reference value among all sampled comets.

Table 5. Median values mixing ratios for comets.

	CH_3OH	HCN	NH_3	H_2CO	C_2H_2	C_2H_6	CH_4	CO
All[a]	1.95	0.22	0.61	0.16	0.08	0.49	0.82	2.18
JFCs[b]	1.58	0.22	0.61	0.22	0.08	0.31	0.54	1.77

a. Median values for "all" sampled comets ("all" = OCCs + JFCs). Considered values for OCC mixing ratios are listed in Dello Russo et al. 2016, Table 3. Values for mixing ratios in JFCs are listed in Paganini et al. 2019, Table 3.
b. Median values for JFCs listed in Paganini et al 2019, Table 3.

Ethane provides some of the brightest emission features in the infrared 3.4 μm wavelength region and multiple emission lines from the ν_7-band were detected during the overall observing campaign. Like CO, ethane is a hyper-volatile specie. Both molecules are *apolar*, therefore very

movable, so we could expect they could easily escape following a similar outgassing trend, if uniformly distributed. Based on absolute values of production rates shown in Figure 5 (panel E and F) and its abundances relative to water in Figure 6 (panel b), ethane in 21P/G-Z looks pretty much constant in our observations, except for a small increase on 8th – 9th August during the second pre-perihelion run.

Figure 5 indeed shows clearly that while absolute values of production rates for water and CO decrease by about 49% and 22% respectively relative to their reference values (weighted mean of measurements), scaled to unity, C_2H_6 increases by about 36%. Interestingly, despite their common apolar nature and their volatility, the absolute outgassing rates of ethane in 21P do not appear to be correlated with CO nor to water. A similar trend is observed in their mixing ratios during our observing campaign (Figure 6). While CO mixing ratios (consistent with the JFCs) remained constant during our observations, ethane appears to be slightly depleted relative to the median reference value for JFCs [C_2H_{6JFC} = 0.31, Figure 6, black line], except for the second pre-perihelion observing run (8th and 9th Aug), when it showed an enhanced abundance. This increase in the C_2H_6 mixing ratio could have been related to lower water outgassing on that date, or a possible outburst event driven by ethane. Another tentative explanation could be the presence of a sort of rotational effect which is consistent with a macroscopic heterogeneous composition of the 21P nucleus, with some regions being richer than others in ethane compared with water.

Compared to the median reference value among all sampled comets [$C_2H_{6\,all}$ = 0.49, Figure 6, blue line], ethane appears to be depleted, except for the second pre-perihelion observing night when it is consistent.

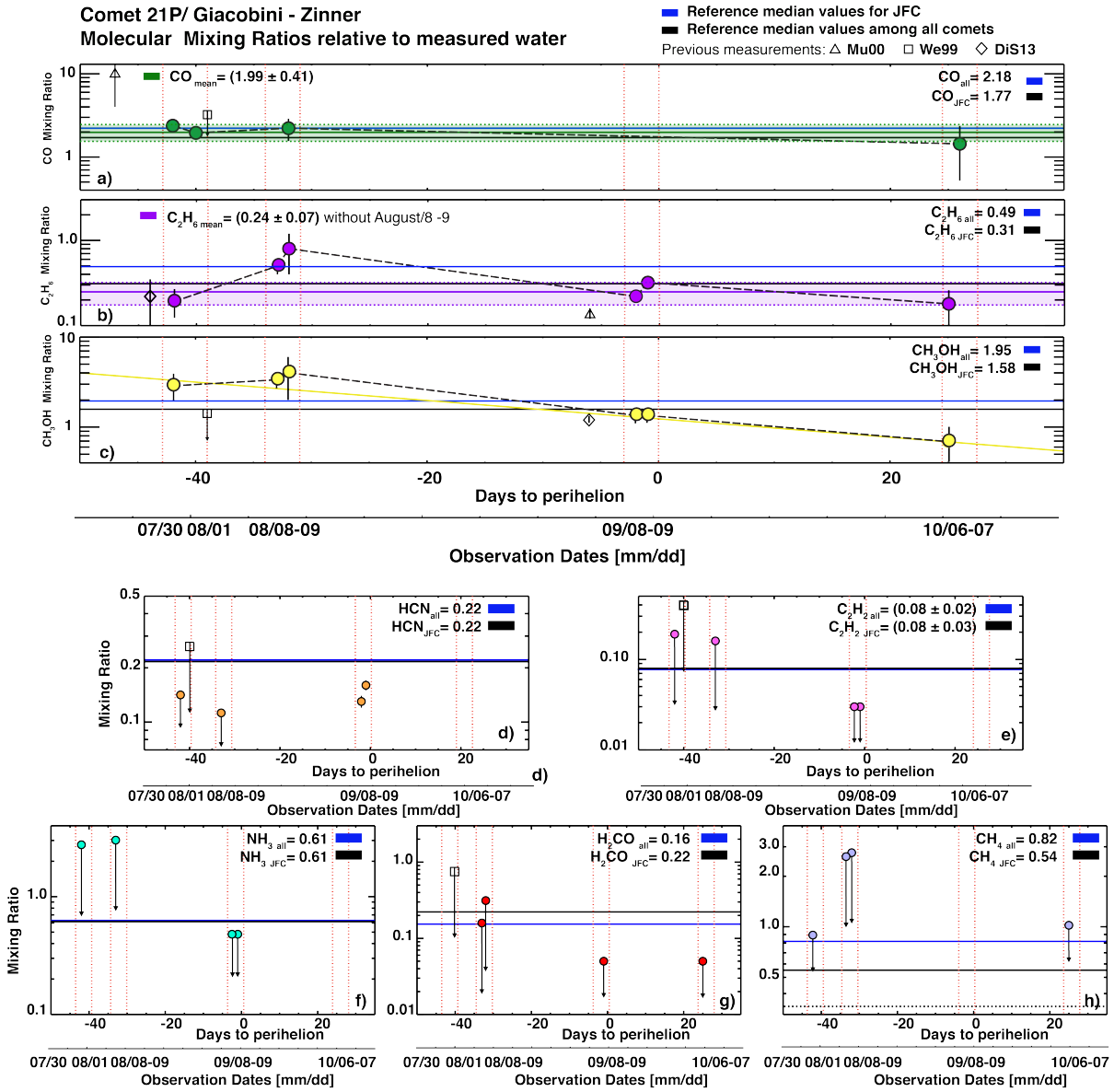

Figure 6 – Mixing ratios of primary volatiles in 21P/Giacobini-Zinner.
In this graphic, temporal behavior of molecular mixing ratios in 21P/G-Z are shown. In each panel mixing ratios relative to measured water are shown in different colors and are compared with the median reference value for JFCs (black line) and median reference value among all sampled comets (blue line). On the x-axis, both "days to perihelion passage" and "observation dates" are reported. On the y-axis molecular abundances of each detected species are reported. Panel (a) shows CO mixing ratios measured with iSHELL (green dots), the weighted mean value and error (green line and shadow) across the observing campaign and also reports previous measurements performed by Mumma et al. (2000) and Weaver et al. (1999) for comparison (triangles and squares respectively). Panel (b) shows ethane mixing ratios measured with iSHELL (purple dots), the weighted mean value and error (purple line and shadow), and previous measurements reported by DiSanti et al. (2013) & Mumma et al. (2000) (diamonds and triangles respectively). Panel (c) shows methanol mixing ratios measured with iSHELL (yellow dots) and their possible seasonal trend (yellow line), along with the previous measurements reported by (DiSanti et al. 2013) and Weaver et al. (1999) (diamonds and squares respectively). Finally, panel (d), (e), (f), (g) and (h) report hydrogen cyanide, acetylene, formaldehyde mixing ratios (or upper limits) measured with iSHELL (orange, pink, cyan, red and light purple dots respectively), and previous upper limits (squares) reported by Weaver et al. (1999).

3.2.2 The case of CH_3OH

Methanol could be efficiently produced from CO-ices on grain surfaces through low temperature hydrogen addition chemistry (Charnley and Rodgers 2009 and references therein). The reaction chain initially forms the highly reactive HCO radical and then formaldehyde and methanol. Although we could expect the CH_3OH molecular abundance in comets to depend on the efficiency of chemical reactions and the cosmogonic abundance of CO-ices on the pre-cometary grains, it is not actually a straightforward process to relate the measured molecular abundances in comets to the primordial chemical processing that occurred on the protoplanetary grains.

In 21P/G-Z the methanol ν_2-band was sampled in orders 155 and 154 of the Lp1 and L3 iSHELL setting. We detected methanol during each observing run and its production rates are reported in Figure 5, panels G and H, and its abundances relative to water in Figure 6, panel (c). Interestingly, in the pre-perihelion observing runs methanol appears to be overabundant relative to both the median JFCs reference value [CH_3OH_{JFC} = 1.58, Fig. 6, black line], and to the median reference value among all sampled comets [CH_3OH_{all} = 1.95, Fig. 6, blue line]. However, later observations showed decreasing CH_3OH mixing ratios, until it appears somewhat depleted relative to (both) reference values (mixing ratio values are reported in Table 4, last column). This reported trend is consistent with a possible seasonal effect. As already mentioned, we do not have enough significant measurements to properly trace the mixing ratio evolution across the perihelion passage, but even with these few points the tendency appears clear.

Also, in this case, we note that when water production showed a decrease on 8th-9th August, the methanol mixing ratio experienced a small enhancement. Like the ethane mixing ratio, methanol did not appear to follow outgassing of either water or CO.

3.2.3 Detections of HCN and upper-limits for C_2H_2, NH_3, H_2CO and CH_4

HCN was detected on 8th and 9th September when 21P/G-Z was at a geocentric distance of about 0.39 au, closer to Earth than in our other observing runs. Thus, our detection of hydrogen cyanide is the first reported for 21P/G-Z; previous investigations achieved only upper limits. In Figure 6 panel (d), the molecular mixing ratios (and upper limits) of HCN are presented and compared to the reference median value for JFCs comets and the median value obtained among

all sampled comets. HCN mixing ratios appear to be depleted relative to both the median JFCs reference value (black line) and the median reference value for all sampled comets (blue line).

We did not detect ammonia, acetylene, formaldehyde and methane, so we report their upper limits (3-σ) in Table 4 (also see Figure 6, panels (e), (f), (g) and (h)). As was done for the detected species, the corresponding mixing ratios of C_2H_2, NH_3, H_2CO and CH_4 are shown and compared with the median reference values for JFC comets and the median value obtained among all sampled comets.

For a specific molecule, the 3-σ upper limit production rate measurement for each observing night is obtained combining together the 1σ–errors over multiple spectral orders of a specific iSHELL setting. For example, considering that ammonia is usually targeted in orders 171 and 173 of setting L1, we extracted the 1-σ limit for its production rate measurement throughout our Levenberg-Marquardt fitting method for those spectral orders, and then we combined them as the weighted mean error. We finally computed our 3-σ upper limit as 3 times the 1-σ weighted mean error. As expected, in general 3-σ upper limits are smaller (more significant) for the two nights near-perihelion passage (run three on 8th and 9th September) than in the pre- and post-perihelion phases. The near-perihelion run returned better signal-to-noise in our spectra owing to the closer proximity of 21P to Earth, compared with the other observing runs. This can be noted in Figure 6 panels (e), (f), and (g) where C_2H_2, NH_3, and H_2CO 3-σ upper limits are higher in the pre-perihelion runs than at the perihelion observations.

Even with a 3-σ upper limit, the acetylene and formaldehyde mixing ratios at perihelion passage appear significantly depleted relative to the median reference value for JFCs (black line) and relative to the reference value for all sampled comets (blue line), however, we cannot claim the same for ammonia.

During the very favorable 2018 perihelion passage 21P/G-Z has been broadly studied with different techniques and at different wavelength ranges. The comparison of measurements obtained with such different methods of investigation allows an exhaustive understating of the chemistry and molecular composition of this comet. From the 2018 multi-instrument optical observing campaign conducted at the Lowell Observatory, Schleicher et al. reported a strong asymmetry in the production rates of radicals such as CN, OH, C_3 and C_2 across the perihelion passage confirming the inhomogeneous and peculiar nature of 21P/G-Z (Schleicher et al. 2018). Our detections of HCN only at the perihelion passage and 3-σ upper limits for C_2H_2 throughout

the campaign prevent a full picture on the chemical evolution of such parent molecules and from the comparison with optical measurements. High signal-to-noise detections are essential to properly evaluate possible variations in HCN and C_2H_2 production rates and to compare them with their possible fragment radical candidates CN and C_2.

However, investigations of C_2H_2 and HCN, have been of great relevance in order to quantify the depletion of C_2 relative to CN in this comet seen at optical wavelengths. As mentioned, 21P/G-Z was defined as the *archetype of the carbon-chain depleted comets* among the overall population of sampled comets (A'Hearn et al. 1995, Cochran et al. 1992, Fink 2009, Cochran et al. 2015). Following the approach in A'Hearn et al. (1995), mixing ratios can be expressed as the logarithm of the ratio between the production rates of two molecular species. Usually, based on optical measurements of radicals, comets are defined to be *carbon-chain typical* when they are characterized by a value of $\log[Q(C_2)/Q(CN)]$ between -0.09 and 0.29. *Carbon-chain depleted* comets are instead characterized by a value between -1.22 and -0.21. Our measurements of HCN and 3-σ upper limits of C_2H_2, considered candidates for native precursors of the C_2 and CN radicals, revealed a maximum value of -0.739 for $\log[3\text{-}\sigma(C_2H_2) / Q(HCN)]$, thereby classifying and confirming the carbon-chain depleted nature of this comet, in agreement with previous measurements (e.g. Schleicher et al. 1987, A'Hearn et al. 1995, DiSanti et al. 2013, Cochran et al. 2015).

Methane (3-σ) upper limits are evaluated in the pre- and post-perihelion observations: on 31st July and on 8th - 9th August, and in the post-perihelion phase on 6th October, when the comet had a geocentric velocity high enough to shift the cometary emission lines from their telluric counterparts. The values reported for the 31st July and the 6th October observing runs are consistent, while on 8th - 9th August we clearly see higher values. This observed decrease in sensitivity of our achieved 3-σ upper limits (i.e., a higher value than from the other observing runs) could derive from the lower value for $Q(H_2O)$ measured on that date, in turn leading to higher limits for trace gas mixing ratios (Figure 5, panels A and B.

4. Conclusions

The volatile composition of 21P/Giacobini-Zinner, described as one of the brighter comets of Jupiter's dynamical family, has been measured and presented.

Comet 21P/G-Z was observed previously at infrared wavelengths, but a characterization of its volatile composition was far from complete (Weaver et al. 1999; Mumma et al. 2000; DiSanti et al. 2013). In this work we present measurements of primary species such as water, ethane, methanol, carbon monoxide, acetylene, hydrogen cyanide and formaldehyde collected during its favorable apparition in 2018.

We followed comet 21P/G-Z during its perihelion passage, in four distinct observing runs. The first two pre-perihelion runs were in late July and early August, and specifically on 30th July – 1st August, and on 8th – 9th August, the third run was on 8th – 9th September immediately before the perihelion passage (10th September 2018), and the post-perihelion run was on 6th – 7th of October 2018. Thus, this work enhances previous chemical investigations on 21P, by reporting on its molecular outgassing at different heliocentric distances (pre- and post-perihelion).

Water emission lines were detected on all observing nights, using setting M1 and L1c of iSHELL. The strongest water detections were obtained during the perihelion passage, on 8th – 9th September 2018, when we observed 71 water lines from seven vibrational non-resonance fluorescence bands. Water production rates seemed to be almost constant throughout our observing campaign (within the confidence limits), except for an outgassing anomaly during the pre-perihelion observing runs (1st August, and 8th-9th August). CO emission lines were detected in the pre- and post-perihelion phases when the cometary geocentric velocity was sufficiently high to shift the cometary emission lines from their telluric counterparts. CO molecular abundances relative to water appeared to be constant during the observing campaign, consistent with a possible correlation between water and CO outgassing. If confirmed by future observations, this possible correlation would be really interesting due to the polar and stable nature of water and the apolar and volatile nature of CO. An intriguing explanation would be the presence of an intimate mixture of water and CO ices, formed by co-deposition at very low temperatures but with current sublimation of both controlled by water ice. The very low abundance of CO relative to water is consistent with this concept.

Ethane mixing ratios relative to water showed a constant depleted behavior for most observing nights, except for one run (8th-9th August) in which we observed significant enhancement. Three possible explanations of such behavior have been considered: (1) a possible outburst of ethane could explain this enhancement, or (2) decrease of water outgassing on those specific nights or (3) it could be the effect of rotational variation stemming from heterogenous

composition of the nucleus Last statement could be verified only with the addition of complementary observations performed by other teams (e.g. Roth et al. 2018).

Methanol molecular abundances appear to be overabundant in the pre-perihelion runs, followed by a constant decrease to somewhat depleted values in the post-perihelion phase. This behavior was suggested to be due to a possible seasonal effect.

Finally, 3-σ upper limits for acetylene and detections of hydrogen cyanide confirmed their expected depletion relative to values in other comets not depleted in C_2/CN at optical wavelengths, if C_2H_2 and HCN are the principal precursors for C_2 and CN in 21P/Giacobini-Zinner. The infrared results of the putative primary volatiles are thus consistent with measurements of these product species at optical wavelengths.

The presented molecular abundances in 21P confirmed the interesting depleted and heterogenic composition of this comet, previously revealed in the 1998 and 2005 apparitions. Molecular mixing ratios presented and discussed in this work are in agreement with results from previous observations listed in Table 1 and graphed in Figure 5. In the figure, measured mixing ratios of CO, C_2H_6, CH_3OH and HCN (at perihelion) are shown together with previous measurements performed at similar heliocentric distances by Mumma et al. (2000), Weaver et al. (1999), and DiSanti et al. (2013). The 3-σ mixing ratios of HCN (pre-perihelion), C_2H_2 and H_2CO reported here are consistent with 3-σ upper limits obtained in previous apparitions.

Our discussion is based on eight observing nights, and of course, the lack of a fully sampled chemical evolution across the pre-perihelion and post-perihelion observations surely limits our ability to characterize the volatile composition of 21P/G-Z. The addition of contemporary observations at multiple wavelengths by other teams is of extreme importance to achieve a more complete picture of its chemical taxonomy and possible evolution during this apparition.

Acknowledgments

For part of this work, S.F. was supported by the NASA Postdoctoral Program at the NASA Goddard Space Flight Center, administered by Universities Space Research Association (USRA) under contract with NASA. The NASA Astrobiology Institute supported this work through award 13-13NAI7-0032 to the Goddard Center for Astrobiology. The authors thank the NASA Infrared Telescope Facility (IRTF) Director J. Rayner and the supporting staff for their outstanding

operational support and valuable technical suggestions during the observing campaign. S.F. thanks Rolando Ligustri (Udine, Italy) for the wonderful pictures of comet 21P/Giacobini-Zinner taken with the iTelescope T5 in New Mexico.

References

A'Hearn, M. F., Millis, R. C., Schleicher, D. O., Osip, D. J., & Birch, P. V. 1995, Icarus, 118, 223

Bockelée-Morvan, D, and Biver, N. 2017, Phil. Trans. R. Soc. A 375: 20160252.

Bonev, B. P. 2005, Towards a Chemical Taxonomy of Comets: Infrared Spectroscopic Methods for Quantitative Measurements of Cometary Water (The University of Toledo: Ph.D. Thesis), 322

Cochran, A. L., & Barker, E. S. 1987, Astronomical Journal, 93, 239

Cochran, A. L., Barker, E. S., & Gray, C. L. 2012, Icarus 218, 144.

Cochran, A. L., Barker, E. S., Ramseyer, T. F., & Storrs, A. D. 1992, Icarus (ISSN 0019-1035), 98, 151

Cochran, A. L., Levasseur-Regourd, A.-C., Cordiner, M., et al. 2015, Space Sci Rev, 197 (Springer Netherlands), 9-46

Dello Russo, N., DiSanti, M. A., Mumma, M. J., Magee-Sauer, K., & Rettig, T. W. 1998, Icarus, 135, 377

Dello Russo, N., Kawakita, H., Vervack, R. J., & Weaver, H. A. 2016, Icarus, 278, 301

DiSanti, M. A., Bonev, B. P., Magee-Sauer, K., et al. 2006, Astrophys J, 650, 470

DiSanti, M. A., Bonev, B. P., Villanueva, G. L., & Mumma, M. J. 2013, Astrophys J, 763, 1

DiSanti, M. A., Mumma, M. J., Dello Russo, N., & Magee-Sauer, K. 2001, Icarus, 153, 361

Ehrenfreund, P., & Schutte, W. A. 2000, Space Infrared Telescopes and Related Science, 25, 2177

Ehlert, S., Moticska, N., & Egal, A. 2019, Astronomical Journal, 158:7

Faggi, S., Villanueva, G. L., Mumma, M. J., & Paganini, L. 2018, Astronomical Journal, 156, 68

Fink, U., 2009, Icarus 201, 311.

Fink, U., & Hicks, M. D. 1996, Astrophys J, 459, 729

Gérard, E., Bockelée-Morvan, D., Bourgois, G., Colom, P., & Crovisier, J. 1988, Astronomy and Astrophysics Supplement Series (ISSN 0365-0138), 74, 485

Gloeckler, G., Hovestadt, D., Ipavich, F. M., et al. 1986, Geophys Res Lett, 13, 251

Hanner, M. S., Veeder, G. J., & Tokunaga, A. T. 1992, Astronomical Journal (ISSN 0004-6256), 104, 386

Kawakita, H., Ootsubo, T., Shinnaka, Y., et al. 2018, American Astronomical Society, 50, 210.10

Lara, L. M., Licandro, J., Oscoz, A., & Motta, V. 2003, A&A, 399, 763

McFadden, L. A., A'Hearn, M. F., Feldman, P. D., et al. 1987, Icarus (ISSN 0019-1035), 69, 329

Mumma, M. J., and Charnley, S. B. 2011, Ann. Rev. Astron. Astrophys. 49:471-524.

Mumma, M. J., DiSanti, M. A., Dello Russo, N., et al. 2000, Astrophys J, 531, L155

Mumma, M. J., DiSanti, M. A., Dello Russo, N., et al. 2003, Adv Space Res, 31, 2563

Paganini, L., Mumma, M. J., Villanueva, G. L., et al. 2014, Astrophys J, 791 122

Paganini, L., Camarca, M. N., Mumma, M. J., et al. 2019, Astronomical Journal, 158:98

Pittichova, J., Woodward, C. E., Kelley, M. S., & Reach, W. T. 2008, arXiv.org, Vol. astro-ph (IOP Publishing), 1127

Rayner, J., Bond, T., Bonnet, M., et al. 2012, eds. I. S. McLean, S. K. Ramsay, & H. Takami, Vol. 8446 (SPIE), 84462C

Rodgers, S. D., & Charnley, S. B. 2003, Astrophys J, 585, 355

Roth, N. X., Gibb, E. L., Bonev, B. P., et al. 2018, AJ, 156, 251

Roth, N., Gibb, E., Dello Russo, N., et al. 2018, American Astronomical Society, 50, 210.11

Schleicher, D. G., Millis, R. L., & Birch, P. V. 1987, Astronomy and Astrophysics (ISSN 0004-6361), 187, 531

Schleicher, D., & Knight, M. 2018, American Astronomical Society, 50, 210.12

Slavin, J. A., Goldberg, B. A., Smith, E. J., et al. 1986a, Geophys Res Lett, 13, 1085

Slavin, J. A., Smith, E. J., Tsurutani, B. T., et al. 1986b, Geophys Res Lett, 13 (John Wiley & Sons, Ltd), 283

Telesco, C. M., Decher, R., Baugher, C., et al. 1986, Astrophysical Journal, 310, L61

Villanueva, G. L., Magee-Sauer, K., & Mumma, M. J. 2013a, J Quant Spectrosc Radiat Transfer, 129, 158

Villanueva, G. L., Mumma, M. J., & Magee-Sauer, K. 2011b, J Geophys Res Pl, 116, 1

Villanueva, G. L., Mumma, M. J., Bonev, B. P., et al. 2012b, J Quant Spectrosc Radiat Transfer, 113, 202

Villanueva, G. L., Mumma, M. J., DiSanti, M. A., et al. 2011a, Icarus, 216, 227

Villanueva, G. L., Mumma, M. J., DiSanti, M. A., et al. 2012a, Icarus, 220, 291

Villanueva, G. L., Mumma, M. J., Novak, R. E., et al. 2013b, Icarus, 223 (Elsevier Inc.), 11

Villanueva, G. L., Smith, M. D., Protopapa, S., Faggi, S., & Mandell, A. M. 2018, J Quant Spectrosc Radiat Transfer, 217, 86

Weaver, H. A., Chin, G., Bockelée-Morvan, D., et al. 1999, Icarus, 142, 482

Xie, X., & Mumma, M. J. 1996, Astrophys J, 464, 457

Yamamoto, T. 1985, Astron. & Astrophys. 142, 31-36